









## Cation and anion topotactic transformations in cobaltite thin films leading to Ruddlesden-Popper phases

I-Ting Chiu,<sup>1</sup> Min-Han Lee ,<sup>2,3</sup> Shaobo Cheng,<sup>4</sup> Shenli Zhang ,<sup>5</sup> Larry Heki,<sup>6</sup> Zhen Zhang,<sup>7</sup> Yahya Mohtashami,<sup>8</sup> Pavel N. Lapa,<sup>3</sup> Mingzhen Feng ,<sup>9</sup> Padraic Shafer,<sup>10</sup> Alpha T. N'Diaye,<sup>10</sup> Apurva Mehta ,<sup>11</sup> Jon A. Schuller,<sup>8</sup> Giulia Galli ,<sup>5,12</sup> Shriram Ramanathan,<sup>7</sup> Yimei Zhu ,<sup>4</sup> Ivan K. Schuller ,<sup>2,3</sup> and Yayoi Takamura ,<sup>9,\*</sup>

<sup>1</sup>Department of Chemical Engineering, University of California, Davis, Davis, California 95616, USA

<sup>2</sup>Materials Science and Engineering Program, University of California, San Diego, La Jolla, California 92093, USA

<sup>3</sup>Department of Physics and Center for Advanced Nanoscience, University of California, San Diego, La Jolla, California 92093, USA

<sup>4</sup>Condensed Matter Physics and Materials Science Division, Brookhaven National Laboratory, Upton, New York, 11973, USA

<sup>5</sup>Pritzker School of Molecular Engineering, The University of Chicago, Chicago, Illinois 60637, USA

<sup>6</sup>Materials Department, University of California, Santa Barbara, Santa Barbara, California 93106, USA

<sup>7</sup>School of Materials Engineering, Purdue University, West Lafayette, Indiana 47907, USA

<sup>8</sup>Department of Electrical and Computer Engineering, University of California, Santa Barbara, Santa Barbara, California 93106, USA

<sup>9</sup>Department of Materials Science and Engineering, University of California, Davis, Davis, California 95616, USA

<sup>10</sup>Advanced Light Source, Lawrence Berkeley National Laboratory, Berkeley, California 94720, USA

<sup>11</sup>Stanford Synchrotron Radiation Lightsource, SLAC National Accelerator Laboratory, Menlo Park, California 94025, USA

<sup>12</sup>Materials Science Division and Center for Molecular Engineering, Argonne National Laboratory, Lemont, Illinois 60439, USA



(Received 31 March 2021; accepted 13 May 2021; published 24 June 2021)

Topotactic transformations involve structural changes between related crystal structures due to a loss or gain of material while retaining a crystallographic relationship. The perovskite oxide  $\text{La}_{0.7}\text{Sr}_{0.3}\text{CoO}_3$  (LSCO) is an ideal system for investigating phase transformations due to its high oxygen vacancy conductivity, relatively low oxygen vacancy formation energy, and strong coupling of the magnetic and electronic properties to the oxygen stoichiometry. While the transition between cobaltite perovskite and brownmillerite (BM) phases has been widely reported, further reduction beyond the BM phase lacks systematic studies. In this paper, we study the evolution of the physical properties of LSCO thin films upon exposure to highly reducing environments. We observe the rarely reported crystalline Ruddlesden-Popper phase, which involves the loss of both oxygen anions and cobalt cations upon annealing where the cobalt is found as isolated Co ions or Co nanoparticles. First-principles calculations confirm that the concurrent loss of oxygen and cobalt ions is thermodynamically possible through an intermediary BM phase. The strong correlation of the magnetic and electronic properties to the crystal structure highlights the potential of utilizing ion migration as a basis for emerging applications such as neuromorphic computing.

DOI: [10.1103/PhysRevMaterials.5.064416](https://doi.org/10.1103/PhysRevMaterials.5.064416)

### I. INTRODUCTION

Ion migration-induced modification of physical properties is an emerging research direction in the search for tunable materials that can revolutionize the growing field of neuromorphic computing [1–3]. Among the candidate materials, perovskite oxides with the chemical formula  $\text{ABO}_3$  are of interest because of their wide range of physical properties, high oxygen ion conductivities, and the multitude of related phases such as the Grenier ( $\text{ABO}_{2.7}$ ), brownmillerite (BM,  $\text{ABO}_{2.5}$ ), square planar (SP,  $\text{ABO}_2$ ) [4,5], and Ruddlesden-Popper (RP,  $\text{A}_{n+1}\text{B}_n\text{O}_{3n+1}$  where  $n = \text{integer}$ ) [6,7] phases. Previous studies on these materials have focused on the impact of the A and B stoichiometry [8,9]; however, recent studies have turned to the oxygen stoichiometry, where topotactic transformations can occur between related structural phases due to a loss or

gain of oxygen ions, while retaining a relationship in the crystallographic orientation [10–12]. Relative to the parent perovskite phase, oxygen deficiency  $\delta$  (where  $0 < \delta < 1$ ) is accommodated by a lowering of the average B-ion valence state and a change in the local coordination environment from corner-shared  $\text{BO}_6$  octahedra in the perovskite phase, to alternating layers of  $\text{BO}_6$  octahedra and  $\text{BO}_4$  tetrahedra in the BM phase [see structural diagrams in Figs. 1(k) and 1(m)]. Further reduction from the BM phase can lead to an in-plane  $\text{BO}_4$  coordination in the SP phase, or even one of the RP phases, where both B and oxygen ions are partially depleted from the parent perovskite phase. As a result, these structural changes lead to substantial modification to the physical properties.

A gradual progression between the perovskite and BM phases have previously been demonstrated in several complex oxide systems, including  $\text{La}_{0.7}\text{Sr}_{0.3}\text{CoO}_3$  (LSCO) [13,14],  $\text{La}_{0.67}\text{Sr}_{0.33}\text{MnO}_3$  [15], and  $\text{YBa}_2\text{Cu}_3\text{O}_{7-\delta}$  [16], by the deposition of ultrathin Gd layers of varying thickness. The

\*Corresponding author: [ytakamura@ucdavis.edu](mailto:ytakamura@ucdavis.edu)

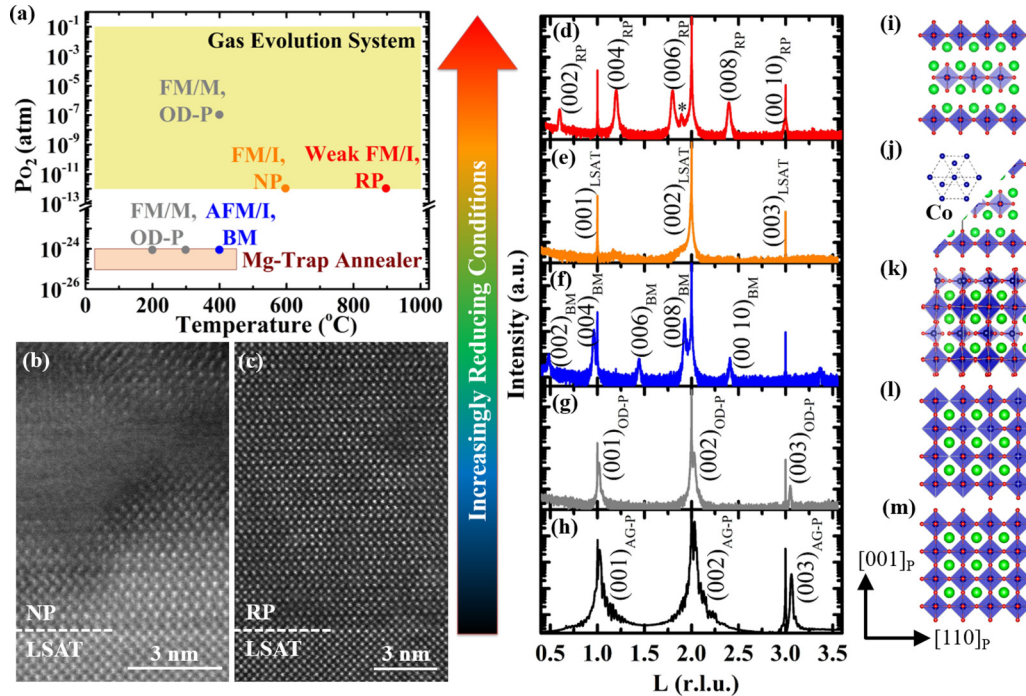


FIG. 1. (a) Phase diagram of the structural, magnetic, and electrical properties of LSCO films exposed to anneals under highly reducing conditions. (b) and (c) High-angle annular dark field (HAADF) scanning transmission electron microscopy (STEM) images of the nanoparticle (NP) and Ruddlesden-Popper (RP) samples, respectively. (d)–(h) X-ray diffraction (XRD) curves and (i)–(m) crystal structure diagrams for the annealed LSCO films. The XRD curves show sharp, high intensity peaks arising from the LSAT substrate and weaker film peaks arising from the  $(00L)$  planes of the respective structure. In (d), the \* peak results from the sample holder. In (i)–(m), the green and red atoms represent La/Sr and oxygen ions, respectively, while Co ions (blue) sit in the center of the octahedra/tetrahedra. As shown in (j), this NP phase consisted of both the polycrystalline grains of the RP phase and metallic Co nanoparticles. The metallic Co NPs are not observed due to their small size, low density, and/or their misalignment relative to the zone axis of the image.

Gd getter layer experiences a spontaneous redox reaction to form  $\text{GdO}_x$ , leaching oxygen ions from the underlying complex oxide thin films and resulting in a topotactic transformation, which then leads to a change in the magnetic and electrical properties in these complex oxides. Other studies focused on the  $\text{SrFeO}_{3-\delta}$  and  $\text{SrCoO}_{3-\delta}$  systems where a reversible transformation between the stable BM  $\text{SrFeO}_{2.5}$  ( $\text{SrCoO}_{2.5}$ ) phase and the metastable  $\text{SrFeO}_3$  ( $\text{SrCoO}_3$ ) perovskite phase was observed with an applied electrical field or under optimized oxidizing annealing conditions [1, 11, 17–20]. With further reduction, BM  $\text{SrFeO}_{2.5}$  films could transform to the infinite-layer  $\text{SrFeO}_2$  SP phase [19, 21]. However, in the cobaltite system, further reduction of BM  $\text{SrCoO}_{2.5}$  films led to amorphous films or nano-twinned, tetrahedrally coordinated phases [20, 22] rather than the formation of the  $\text{SrCoO}_2$  SP phase or even the  $\text{Sr}_2\text{CoO}_4$  [23, 24] RP phase. Therefore, in this paper, we investigate the mechanisms and the phase stability associated with cobaltite topotactic transformations.

A series of topotactic transformations were initiated in Sr-doped lanthanum cobaltite ( $\text{La}_{0.7}\text{Sr}_{0.3}\text{CoO}_{3-\delta}$ ) thin films exposed to anneals under highly reducing conditions. At this Sr-doping level, the perovskite phase is the equilibrium phase, characterized by coincident metal-to-insulator and ferromagnetic (FM)-to-paramagnetic (PM) transitions at the Curie temperature  $T_C \sim 240$  K [25], a high oxygen vacancy conductivity, and relatively low oxygen vacancy formation energy [26]. The anneals were performed using either a Mg-trap

annealing system [27] or a gas evolution system [28], which enabled the exploration of wide temperature/pressure phase space ranging from room temperature to 1000 °C and oxygen partial pressures from  $10^{-25}$  to  $10^{-1}$  atm [see Fig. 1(a)]. X-ray absorption (XA) spectroscopy and scanning transmission electron microscopy (STEM) showed that these structural transformations involved a change of the Co local coordination from a mixture of  $\text{Co}^{3+}/\text{Co}^{4+}$  ions in octahedral coordination in the perovskite phase to  $\text{Co}^{2+}$  ions in octahedral coordination in a  $\text{La}_{1.4}\text{Sr}_{0.6}\text{Co}_{1+\nu}\text{O}_{4-\delta}$  RP phase (where  $0 \leq \nu < 1$  and  $0 < \delta < 1$ ) formed under the most reducing conditions. Raman spectroscopy and first-principles calculations suggest that the formation of the RP phase involves the loss of both oxygen anions and Co ions through an intermediary BM phase. As a result, the magnetic properties evolved between various FM and antiferromagnetic (AFM) phases, and the room temperature resistivity spanned eight orders of magnitude. We successfully observed the formation of the RP phase with its own distinct physical and functional properties. Furthermore, the combination of experiment and theory enabled us to elucidate the formation mechanisms for each of the reduced phases.

## II. EXPERIMENTAL AND THEORETICAL METHODS

Epitaxial LSCO thin films (thickness of 16–28 nm) were deposited on (001)-oriented  $(\text{LaAlO}_3)_{0.3}(\text{Sr}_2\text{TaAlO}_6)_{0.7}$

(LSAT) substrates by pulsed laser deposition with a laser pulse frequency of 1 Hz and laser fluence of  $\sim 0.8 \text{ J cm}^{-2}$ . During the growth, the substrate temperature was held at  $700^\circ\text{C}$ , and the oxygen pressure was 300 mTorr. The films were cooled slowly to room temperature after the deposition with an oxygen pressure of 300 Torr to ensure proper oxygen stoichiometry. The LSCO films were annealed for 1 h either in a gas evolution system which consists of a tube furnace connected to a high vacuum system capable of achieving oxygen partial pressures from  $10^{-12}$  to 0.1 atm and temperatures up to  $1000^\circ\text{C}$  [28] or a Mg-based oxygen trap system capable of achieving oxygen partial pressures down to  $10^{-25}$  atm and temperatures up to  $400^\circ\text{C}$  [27]. In the gas evolution system, the base pressure was maintained at  $\sim 10^{-10}$  atm, and high-purity oxygen ( $>99.99\%$ ) of different pressures ranging from  $10^{-12}$  to  $10^{-7}$  atm was introduced into the annealing chamber using the computer-controlled metal-seated valve [28]. During the Mg-trap annealing experiments, the Mg-based oxygen trap and annealing chamber was maintained at 1 atm total pressure, and the low oxygen partial pressure was generated by flowing ultrahigh purity argon gas through a heated Mg powder bed. The trace amount of oxygen in ultrahigh purity argon reacts with Mg, creating further reduction in the oxygen partial pressure as it flows into the chamber [27]. All pressures quoted in the following sections refer to the oxygen partial pressures  $P_{\text{O}_2}$ .

The structural properties of the films were characterized by x-ray reflectivity (XRR) and high-resolution x-ray diffraction (XRD) using either a Bruker D8 Discover or Rigaku Smartlab four-circle diffractometer using  $\text{Cu } K_{\alpha 1}$  x rays ( $8.04 \text{ keV}$ ). The XRD data for the as-grown perovskite (AG-P) LSCO sample were obtained at Beamline 7-2 at the Stanford Synchrotron Radiation Light Source using an x-ray energy of  $14 \text{ keV}$ . The XRR curves were fit using GenX software to determine the thickness, roughness, and density of the films [29,30]. A Lakeshore cryogenic probe station was used to measure the film resistivity upon warming from  $80 \text{ K}$  with the van der Pauw geometry. The bulk magnetic properties were measured using a Quantum Design VersaLab or Physical Property Measurement System vibrating-sample magnetometer with the magnetic field applied along the in-plane [100] substrate direction. Soft x-ray magnetic spectroscopy at the Co  $L$ -edge was performed at  $80 \text{ K}$  at beamlines 4.0.2 and 6.3.1 at the Advanced Light Source (ALS) using total electron yield detection (which provides surface-sensitive measurements to the top 5–10 nm of the sample), and luminescence yield detection (which probes the full film thickness [31]). The x rays were incident upon the sample at a  $30^\circ$  grazing angle along the in-plane [100] substrate direction. X-ray magnetic circular dichroism (XMCD) spectra were calculated as the difference between XA spectra acquired using right/left circularly polarized x-rays with a  $1.93 \text{ T}$  magnetic field oriented parallel to the propagation direction of the circularly polarized x rays. X-ray linear dichroism (XLD) spectra were calculated as the difference between XA spectra acquired using  $s$ - and  $p$ -polarized x rays such that the x-ray  $\mathbf{E}$  vector is respectively parallel to the in-plane [010] substrate direction or  $30^\circ$  away from the [001] substrate direction, due to the grazing-incidence geometry of the measurements.

High-angle annular dark field (HAADF) STEM images and electron energy loss spectroscopy (EELS) mappings were acquired by a double corrector JEOL ARM 300F TEM. A  $30 \mu\text{m}$  condenser aperture was selected for EELS acquisition. The convergent and collection semi-angles are  $21$  and  $90 \mu\text{m}$ , respectively. The samples used for TEM characterizations were made by standard focus ion beam (FEI Helios NanoLab) lift-out method. Raman spectra were measured at room temperature using a Horiba Jobin Yvon T64000 Raman spectrometer. The excitation light of  $488 \text{ nm}$  was focused onto the sample using a  $100\times$  objective. The signal was collected in a backscattering geometry, and excitation light was blocked by a notch filter. Photoluminescence (PL) spectra were taken using a home-built system coupling an inverted microscope to an imaging spectrometer. The sample was excited with  $405 \text{ nm}$  light under a  $20\times$  objective. Excitation light was rejected by a long-pass filter.

First-principles calculations were performed using the QUANTUM ESPRESSO code (v6.4.1) [32,33], which solves the Kohn-Sham equations of density functional theory (DFT) using plane waves and pseudopotentials. We used DFT +  $U$  ( $U = 3 \text{ eV}$ , as justified in previous calculations) [34], with the Perdew-Burke-Ernzerhof generalized gradient approximation [35] for the exchange-correlation functional and the projected augmented wave pseudopotentials from the PSLibrary [36] (v1.0.0 for La, Sr and O, and v0.3.1 for Co). A previously optimized BM structure [34] was used to calculate the formation energy of Co or O vacancies in the BM phase, which was modeled with a 36-atom orthorhombic cell with the stoichiometry of  $\text{La}_{0.63}\text{Sr}_{0.37}\text{CoO}_{2.5}$ . The initial RP phase was constructed from the  $\text{La}_2\text{CoO}_4$  structure (ID: mp-27494) from the Materials Project [37], where we substituted 37.5% La by Sr in this 28-atom orthorhombic cell. Defective BM structures and the RP structure were then optimized within the orthorhombic lattice symmetry using a plane-wave cutoff of  $1224 \text{ eV}$  and a Monkhorst-Pack k-point grid [38] with the resolution between  $0.02$  and  $0.03 \text{ \AA}^{-1}$ . The convergence thresholds for energy, force, and pressure were set to  $2.0 \times 10^{-4} \text{ eV}$  per formula unit (f.u.),  $0.02 \text{ eV \AA}^{-1}$  per f.u., and  $0.5 \text{ Kbar}$ , respectively.

### III. RESULTS AND DISCUSSION

The range of possible annealing conditions available with the gas evolution and Mg-trap annealing systems is indicated by the shaded regions in Fig. 1(a), while the symbols represent the conditions explored in this paper. Upon exposure to increasingly reducing conditions (i.e., lower oxygen partial pressure and/or higher temperature), the LSCO thin films gradually underwent several topotactic transformations, as revealed through XRR (Fig. S1 in the Supplemental Material [39]) and XRD measurements [Figs. 1(d)–1(h)]. The XRR curves reveal substantial changes in the film thickness, density, and roughness associated with each of these transformations. Tables S1 and S2 in the Supplemental Material [39] list the parameters obtained from fitting the XRR curves using GenX software [29]. For anneals up to  $600^\circ\text{C}/10^{-12} \text{ atm } P_{\text{O}_2}$ , a trend of decreasing density and increasing film thickness and roughness can be observed, as expected for perovskite-related materials with increasing oxygen deficiency [40,41]. The LSCO thin film annealed at  $600^\circ\text{C}/10^{-12} \text{ atm } P_{\text{O}_2}$

experiences a 50.5% increase in the total film thickness (18.6 to 28.0 nm) and 29.9% decrease in the main layer density (6.79 to 4.76 gcm<sup>-3</sup>). Finally, increasing the annealing temperature to 900 °C/10<sup>-12</sup> atm  $P_{O_2}$  leads to a recovery of the film density to 6.28 gcm<sup>-3</sup> (22.6% decrease from the AG-P sample) and roughness, accompanied with a small decrease in thickness to 17.3 nm (5.46% decrease). Therefore, the XRR results suggest that these highly reduced films have experienced substantial structural modification upon annealing.

Analysis of  $\omega$ - $2\theta$  XRD curves [Figs. 1(d)–1(h)] enable the identification of the phases present after each reducing anneal. Reciprocal space maps (Fig. S2 in the Supplemental Material [39]) show that the thin films remain coherently strained to the underlying LSAT substrate regardless of annealing conditions. Figure 1(h) shows the expected series of (00L) peaks for the perovskite phase with an out-of-plane lattice parameter of 3.806 Å. Upon annealing at 200 and 300 °C/10<sup>-24</sup> atm  $P_{O_2}$  as well as 400 °C/10<sup>-7</sup> atm  $P_{O_2}$ , the same series of (00L) peaks can be observed [Fig. 1(g)], indicating that the perovskite phase is maintained. However, the film peaks are shifted to slightly lower  $2\theta$  values than the AG-P phase. For the sample annealed at 400 °C/10<sup>-7</sup> atm  $P_{O_2}$ , the out-of-plane lattice parameter increases slightly to 3.812 Å, which is consistent with the 6.0% decrease in density obtained from the XRR curves and consistent with an oxygen deficient perovskite (OD-P) phase [42,43].

Annealing the LSCO thin films at 400 °C/10<sup>-24</sup> atm  $P_{O_2}$  resulted in the transformation to the BM phase, as characterized by the dramatic shift of the main (00L) film peaks to the low angle side of the LSAT substrate peak, as well as the appearance of prominent half-order peaks due to the quadrupling of the unit cell from the alternating octahedral and tetrahedral layers. The lattice parameter for this BM phase is 16.053 Å. The XRR curves indicate a 6.7% increase in total film thickness and 13% decrease in density accompany the transformation to the BM phase, consistent with prior studies of the perovskite-BM transformation in SrCoO<sub>3- $\delta$</sub>  [1,10,11] and LSCO [13] films. The BM La<sub>0.7</sub>Sr<sub>0.3</sub>CoO<sub>2.5</sub> phase was found to be metastable and slowly transformed back to the perovskite phase over a period of several months at room temperature in air, even when capped with 5 nm Gd/5 nm Au to try to prevent oxygen reincorporation into the film.

Upon annealing at 600 °C/10<sup>-12</sup> atm  $P_{O_2}$ , the film peaks disappear, as shown in Fig. 1(e). This absence of film peaks could be explained by amorphization of the LSCO thin film or the formation of a nano-textured phase where the film breaks up into small crystalline regions in which the planes are not oriented parallel to the substrate surface. HAADF STEM images [Fig. 1(b)] demonstrated that, after annealing, this sample consisted primarily of polycrystalline grains of the RP phase separated by amorphous regions/regions of low crystallinity, or regions misaligned to the zone axis of the image. The out-of-plane lattice parameter of this polycrystalline RP structure is 12.25 ± 0.21 Å, where the (001) planes are not perfectly aligned with the underlying LSAT substrate due to the presence of defects and dislocations at the film-substrate interface. Furthermore, EELS elemental mapping in Fig. 2 demonstrates that this thin film has a nonuniform Co distribution, while maintaining more uniform distributions of the La and O ions. In Fig. 2(e), the Raman spectra showed peaks

at 683, 1366, and 1590 cm<sup>-1</sup>, which can be assigned to the Raman lines of Co nanoparticles (NPs) [44–46]. Therefore, we refer to this sample as the NP sample. The formation of the Co NPs accounts for the loss of Co ions needed to form the RP phase; however, their small size, low density, and/or random orientation precludes their observation in XRD or STEM measurements. Similar effects have been observed in the electrodes of solid oxide fuel cells where nickel particles exsolved from nickel oxides [47,48].

As the LSCO thin films were annealed at 900 °C/10<sup>-12</sup> atm  $P_{O_2}$ , a new epitaxial phase emerged with a pattern of peaks distinct from the perovskite or BM phases. These peaks can be indexed to an out-of-plane lattice parameter of 12.89 Å. A lack of thickness fringes (Fig. S3 in the Supplemental Material [39]) indicates that, compared with the AG-P sample, this phase has large interfacial roughness and  $d$ -spacing variations, further confirmed by XRR in Fig. S1 and Table S2 in the Supplemental Material [39]. HAADF STEM imaging [Fig. 1(c)] confirmed that this sample consists of a single crystalline La<sub>1.4</sub>Sr<sub>0.6</sub>Co<sub>1+v</sub>O<sub>4- $\delta$</sub>  RP structure [7] with an out-of-plane lattice parameter of 12.83 ± 0.05 Å, which is coherently strained to the underlying LSAT substrate. Raman spectra showed that the Co NPs were no longer present; however, PL spectra [Fig. 2(f)] show multi-peaked emission spanning the visible and near-infrared wavelengths (from 480 to 755 nm). Similar spectra have been observed from isolated Co<sup>2+</sup> ions in a variety of host crystals [49–51], suggesting that these PL features also arise from excess Co ions that are generated when the LSCO thin films are reduced. Unlike the BM phase, this RP phase is stable under ambient conditions for a timeframe of years, as determined through XRD measurements.

DFT calculations further support the assignment of the RP phase to the 900 °C annealed sample, as the calculated structural, magnetic, and electronic properties (Table S3 in the Supplemental Material [39]) all showed good agreement with experimental measurements. The computed out-of-plane lattice parameter decreased by 19.5% in the transformation from the BM phase (15.86 Å) to the RP phase (12.76 Å), consistent with the experimentally observed 20% change from BM (16.053 Å) to the 900 °C annealed sample (12.83 Å). A G-type AFM ordering with insulating properties was identified in the calculations with a small net magnetic moment ~0.25  $\mu_B$  per Co ion, consistent with the high resistivity and weak FM properties identified <25 K (as further discussed below). Moreover, our calculated formation energy of cobalt and oxygen vacancies in the BM phase (see Table S4 in the Supplemental Material [39] and the related discussion) revealed that the BM-to-RP phase transition is thermodynamically possible; indeed, we found that the cobalt vacancy requires lower energy to form than the oxygen vacancy in the BM phase, either at the standard condition (27 °C/1 atm) or at the 600 °C/10<sup>-12</sup> atm  $P_{O_2}$  annealing condition, and their formation energies are comparable at the 900 °C/10<sup>-12</sup> atm  $P_{O_2}$  annealing condition. This result indicates that the loss of cobalt and oxygen ions in the BM phase is likely, which is a necessary step to form the RP phase and justifies the appearance of Co NPs detected in experiments.

XA spectra (Figs. 3(a) and S4 in the Supplemental Material [39]) were acquired to detect the change in Co valence state

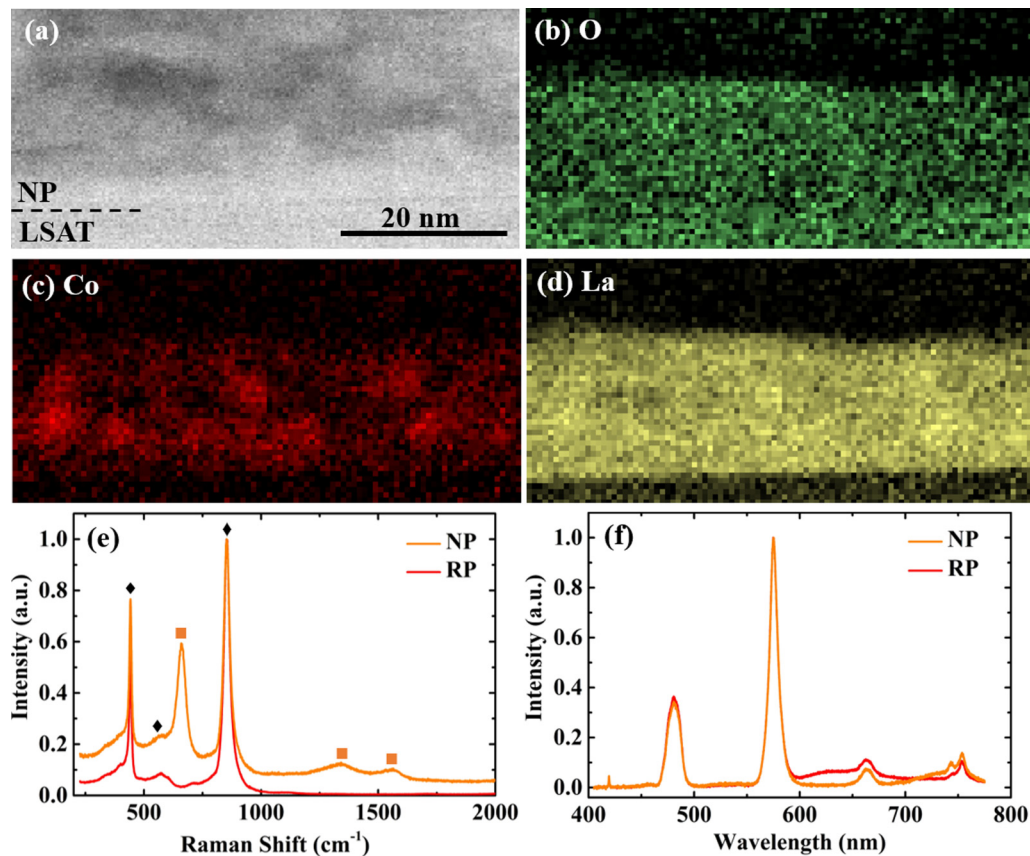


FIG. 2. (a) Electron energy loss spectroscopy (EELS) elemental mapping of the nanoparticle (NP) sample taken at the substrate-film interface showing maps of the (b) oxygen, (c) cobalt, and (d) lanthanum edges. (e) Raman and (f) photoluminescence (PL) spectra of the NP (orange) and Ruddlesden-Popper (RP; red) samples. Raman lines from the LSAT substrate [52] are denoted with black diamond symbols (◆), while those from the cobalt NPs are denoted with orange squares (■). In (f), all PL features arise from the excess Co ions in the NP and RP films.

and local coordination associated with the topotactic transformations. Reference spectra for  $\text{Co}^{2+}$  ions in octahedral coordination ( $\text{CoFe}_2\text{O}_4$  [53]) and metallic Co are included for comparison. The AG-P sample agrees with literature data for mixed valence  $\text{Co}^{3+}/\text{Co}^{4+}$  ion in octahedral coordination [54,55]. The OD-P sample shows only subtle changes compared with the AG-P sample in the form of slightly less defined spectral features. On the other hand, the XA spectra of the highly reduced phases (BM, NP, and RP) show clear signatures of  $\text{Co}^{2+}$  ions in octahedral coordination with subtle differences in the intensities of the three main spectral features denoted with (A)–(C) dotted lines. The decrease in the Co valence state in the highly reduced phases is expected to maintain charge neutrality upon increase in oxygen deficiency  $\delta$ . The subtle spectral differences for the highly reduced phases likely arise from the fact that the Co ions in the BM sample are in mixed octahedral/tetrahedral coordination, while those in the NP and RP samples also have contributions from the Co NPs and isolated Co ions, respectively. In the ideal RP structure with the chemical formula of  $\text{La}_{1.4}\text{Sr}_{0.6}\text{CoO}_4$ , the average Co valence state is  $\text{Co}^{2.6+}$ ; however, our annealed NP and RP samples are likely Co rich with stoichiometry of  $\text{La}_{1.4}\text{Sr}_{0.6}\text{Co}_{1+\nu}\text{O}_{4-\delta}$ , where  $0 \leq \nu < 1$ , resulting in lower average Co valence state.

XMCD measurements at the Co  $L_{3,2}$  absorption edges [Fig. 3(b)] provide complementary information on the element/coordination-specific contributions to the FM properties of the annealed LSCO thin films. Compared with the AG-P sample, the saturation magnetization ( $M_S$ ) of the OD-P films decreased by 60% as the oxygen vacancies break up the  $\text{Co}^{3+}\text{-O}^{2-}\text{-Co}^{4+}$  double exchange network [56,57] and potentially introduces local AFM structures for Co ions near vacancies [34,58]. While the XA spectra for the BM, NP, and RP samples were similar [Fig. 3(a)], stark differences exist in the XMCD spectra. No FM signal was detected for the RP sample at 80 K, and the BM sample showed a weak FM signal with spectral features matching that of  $\text{Co}^{2+}$  ions in octahedral coordination. The XMCD magnitude of the BM sample is only 4.7% of the  $\text{CoFe}_2\text{O}_4$  reference spectra. In contrast, the sample referred to as the NP phase shows a broad negative peak without the multiplet structure typically found in complex oxides and is more reminiscent of metallic Co atoms. Fitting of the XA and XMCD spectra for this sample (Fig. S5 in the Supplemental Material [39]) shows that it can be considered as a mixture consisting of  $\sim 77\%$  of RP phase and  $\sim 23\%$  metallic Co, consistent with the Raman spectra. As shown in Fig. S6 in the Supplemental Material [39], the hysteresis loops show that this phase has a substantially lower coercivity than the AG-P phase (i.e.,  $H_C = 0.1$  T

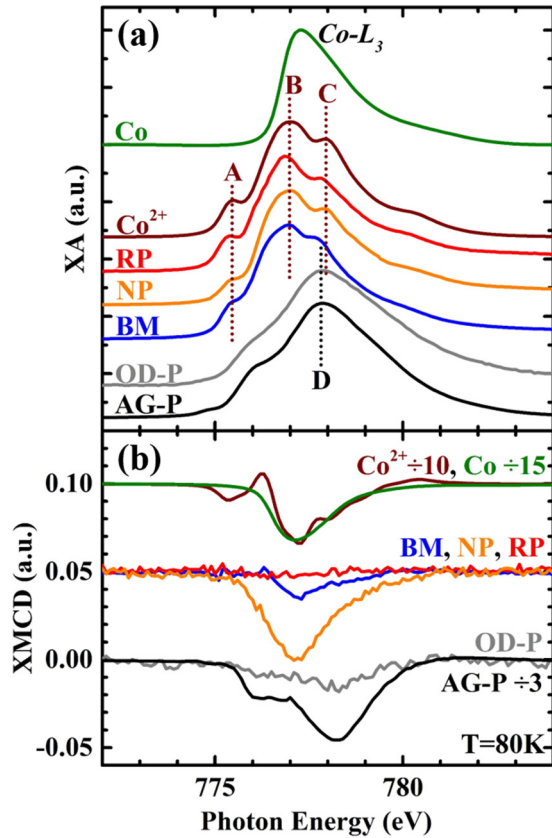


FIG. 3. (a) Co  $L_{3,2}$  x-ray absorption (XA) and (b) x-ray magnetic circular dichroism (XMCD) spectra acquired at 80 K for LSCO thin films after reducing anneals. Reference spectra for  $\text{Co}^{2+}$  ions in octahedral coordination [53] and metallic Co are also included. The XA spectral features of  $\text{Co}^{2+}$  ions are denoted with (A)–(C) dotted lines and the main peak of the  $\text{Co}^{3+}/\text{Co}^{4+}$  ions with a (D) dotted line.

compared with  $H_C \sim 1.25$  T, respectively), consistent with Co NPs [59,60].

The bulk magnetic and electrical properties of the annealed LSCO thin films are shown in Fig. 4. The resistivity data were normalized to the thin film volume, while the magnetization data were normalized to 1. In the resistivity measurement, the transition temperature was determined as the temperature where the curve has a local maximum (i.e.,  $dR/dT = 0$ ) [61,62], while the Curie temperature was determined as the temperature corresponding to the peak in  $|dM/dT|$  [63]. Using these metrics, the transition temperatures are in good agreement between the two measurements. For the AG-P sample, the metal-to-insulator and FM-to-PM transitions coincide at  $T_C \sim 198$  K. The oxygen deficiency in the OD-P phase led to a decrease in  $T_C$  to 180 K and an increase in resistivity across the entire temperature range studied. The increase in resistivity is most dramatic at low temperatures where an additional insulating phase emerges for temperatures  $< \sim 125$  K [64,65]. The highly reduced phases (BM, NP, and RP) had room temperature resistivity values several orders of magnitude higher than the perovskite phases. The high resistivity values for the NP and RP phases prevented resistivity measurements at lower temperatures. The BM phase displayed purely insulating temperature dependence

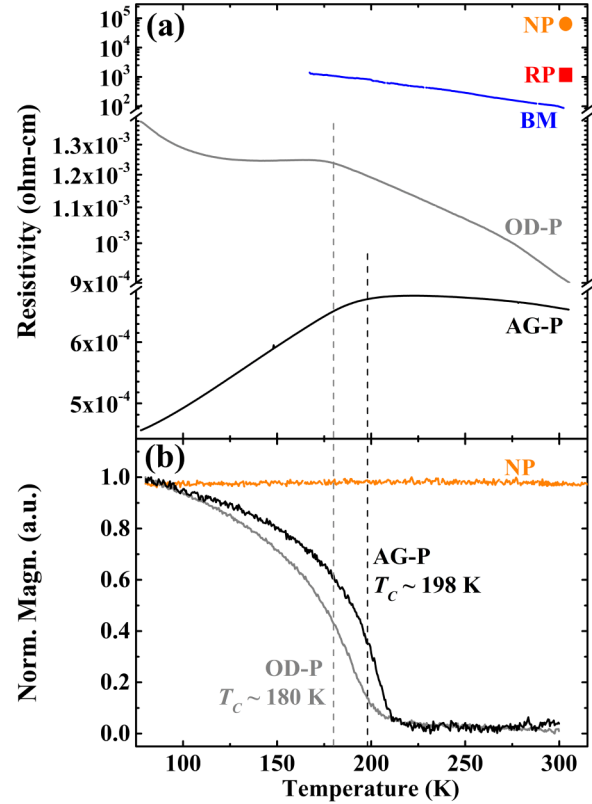


FIG. 4. Film-averaged (a) resistivity and (b) normalized magnetization as a function of temperature for LSCO thin films after reducing anneals. A magnetic field of 0.08 T was applied along the [100] substrate direction during the magnetization measurements.

and no detectable magnetic signal over the temperature range studied, consistent with the AFM properties reported for BM  $\text{SrCoO}_{2.5}$  [66]. XLD measurements suggest that these AFM properties also remain in the  $\text{La}_{0.7}\text{Sr}_{0.3}\text{CoO}_{2.5}$  phase studied here (Fig. S7 in the Supplemental Material [39]) [30,66–69]. The weak FM signal from the BM phase measured in the XMCD spectrum [Fig.3(b) blue curve] was not detected in the magnetization-temperature plot in Fig. 4(b), mainly due to the detection sensitivity difference between the two measurements. In addition to the insulating properties, the NP phase displayed FM properties with a nearly constant magnetization value of  $847 \text{ emu cm}^{-3}$  up to the highest measurement temperature of 370 K. This magnetization value was normalized to the estimated volume of all Co NPs (i.e., 23% of the total NP film volume, based on XA spectra fitting results), and the measured  $M_S$  of these Co NPs corresponds well to the reported value for metallic Co (i.e.,  $M_S = 1352 \text{ emu cm}^{-3}$  compared with  $M_S \sim 1400 \text{ emu cm}^{-3}$  [70,71], respectively). The high  $T_C$  value in the NP sample is also consistent with the presence of FM Co NPs embedded within an insulating matrix. The RP phase has a weak FM phase with low remanent magnetization which appears at temperatures  $< \sim 25$  K (not shown).

Figure 1(a) summarizes the temperature/oxygen partial pressure phase space explored to initiate a wide range of topotactic transformations in perovskite LSCO thin films. Under mild reducing conditions ( $T \leq 300^\circ\text{C}$  at  $10^{-24}$  atm  $P_{\text{O}_2}$ , and  $400^\circ\text{C}$  at  $10^{-7}$  atm  $P_{\text{O}_2}$ ), oxygen deficiency resulted

in a slight expansion of the perovskite unit cell volume, a change in the magnetic properties (decrease in  $T_C$  and  $M_S$ ), and an increase in the resistivity due to the disruption of the  $\text{Co}^{3+}\text{-O}^{2-}\text{-Co}^{4+}$  double exchange network. Increasing the annealing temperature to 400 °C at  $10^{-24}$  atm  $P_{\text{O}_2}$ , resulted in the formation of the BM phase, which displayed AFM/insulator properties with a trace FM signal from  $\text{Co}^{2+}$  ions. This metastable phase slowly transformed back to the perovskite phase over a period of several months in ambient conditions. Annealing at 600 °C/ $10^{-12}$  atm  $P_{\text{O}_2}$  led to the formation of small Co NPs embedded in a polycrystalline matrix of the RP phase characterized by FM/insulator properties by low coercivity and an elevated Curie temperature  $T_C > 370$  K. Notably, this structure was characterized by a dramatic increase in total film thickness (50.5%) and a sharp drop in density ( $-29.9\%$ ) compared with the AG-P thin film. Finally, an epitaxial RP structure ( $a = b = 3.868$  Å,  $c = 12.89$  Å) was obtained after annealing at the most reducing condition explored (900 °C/ $10^{-12}$  atm  $P_{\text{O}_2}$ ). Once formed, this phase remained stable under ambient conditions, and it displayed high resistivity and weak FM properties at temperatures  $< 25$  K with low remanent magnetization.

#### IV. CONCLUSIONS

In summary, a series of topotactic transformations involving the loss of both oxygen anions and cobalt cations were observed in LSCO thin films upon annealing under highly reducing conditions. First-principles calculations were conducted to interpret experiments and characterize the observed phases. These phases not only include the oxygen-deficient perovskite and BM phases, but the RP phase which has been rarely reported in cobaltite topotactic transformations and requires the loss of cobalt cations. A composite phase consisting of FM Co NPs embedded in an insulating RP matrix was observed at an intermediate annealing condition of 600 °C/ $10^{-12}$  atm  $P_{\text{O}_2}$ . These Co NP precipitates redissolved into the oxide matrix upon annealing, forming interstitial Co

ions in the RP phase under the most reducing condition investigated. DFT calculations further confirmed that the formation of the RP phase and Co NPs is thermodynamically possible, and the calculated structural, magnetic, and electronic properties supported the experimental measurements. Each structure possessed its own distinct set of physical properties including FM/metal, AFM/insulator, and two types of FM/insulator phases. The ability to control the physical properties by movement of ion migration suggest their potential for further exploration into the reversibility and order parameter tuning by electric fields for applications such as neuromorphic devices.

#### ACKNOWLEDGMENTS

This work was supported as part of the Quantum Materials for Energy Efficient Neuromorphic Computing, an Energy Frontier Research Center funded by the U.S. Department of Energy (DOE), Office of Science, Basic Energy Sciences under Award No. DE-SC0019273. The Mg-trap annealing experiments were conducted by Z. Zhang supported by AFOSR FA9550-18-1-0250, and the gas evolution system was developed under Award No. FA9550-20-1-0242. This research used resources of the Advanced Light Source, a U.S. DOE Office of Science User Facility under contract no. DE-AC02-05CH11231. Use of the Stanford Synchrotron Radiation Light Source, SLAC National Accelerator Laboratory, was supported by the DOE Office of Science, Office of Basic Energy Sciences under Contract No. DE-AC02-76SF00515. The authors acknowledge the use of the Nanostructures Cleanroom Facility within the California NanoSystems Institute, supported by the University of California, Santa Barbara, and the University of California, Office of the President. Electron microscopy work at BNL and the use of BNLs Center for Functional Nanomaterials are supported by DOE-BES, the Division of Materials Science and Engineering, and Division of Science User Facility, respectively, under Contract No. DE-SC0012704.

- 
- [1] Q. Lu and B. Yildiz, *Nano Lett.* **16**, 1186 (2016).
  - [2] C. Eames, J. M. Frost, P. R. F. Barnes, B. C. O'Regan, A. Walsh, and M. S. Islam, *Nat. Commun.* **6**, 7497 (2015).
  - [3] H.-T. Zhang, Z. Zhang, H. Zhou, H. Tanaka, D. D. Fong, and S. Ramanathan, *Adv. Phys. X* **4**, 1523686 (2019).
  - [4] M. T. Anderson, J. T. Vaughey, and K. R. Poeppelmeier, *Chem. Mater.* **5**, 151 (1993).
  - [5] T. G. Parsons, H. D'Hondt, J. Hadermann, and M. A. Hayward, *Chem. Mater.* **21**, 5527 (2009).
  - [6] M. A. Zurbuchen, W. Tian, X. Q. Pan, D. Fong, S. K. Streiffer, M. E. Hawley, J. Lettieri, Y. Jia, G. Asayama, S. J. Fulk, D. J. Comstock, S. Knapp, A. H. Carim, and D. G. Schlom, *J. Mater. Res.* **22**, 1439 (2007).
  - [7] J. Li *et al.*, *Nano Energy* **78**, 105215 (2020).
  - [8] W. Jian, R. Jia, H.-X. Zhang, and F.-Q. Bai, *Inorg. Chem. Front.* **7**, 1741 (2020).
  - [9] S. Tan, F. Sayed, S. Yang, Z. Li, J. Wu, and P. M. Ajayan, *ACS Mater. Lett.* **1**, 230 (2019).
  - [10] H. Jeon, W. S. Choi, J. W. Freeland, H. Ohta, C. U. Jung, and H. N. Lee, *Adv. Mater.* **25**, 3651 (2013).
  - [11] H. Jeon, W. S. Choi, M. D. Biegalski, C. M. Folkman, I. C. Tung, D. D. Fong, J. W. Freeland, D. Shin, H. Ohta, M. F. Chisholm, and H. N. Lee, *Nat. Mater.* **12**, 1057 (2013).
  - [12] J. Walter, H. Wang, B. Luo, C. D. Frisbie, and C. Leighton, *ACS Nano* **10**, 7799 (2016).
  - [13] D. A. Gilbert, A. J. Grutter, P. D. Murray, R. V. Chopdekar, A. M. Kane, A. L. Ionin, M. S. Lee, S. R. Spurgeon, B. J. Kirby, B. B. Maranville, A. T. N'Diaye, A. Mehta, E. Arenholz, K. Liu, Y. Takamura, and J. A. Borchers, *Phys. Rev. Mater.* **2**, 104402 (2018).
  - [14] G. Rippy, L. Trinh, A. M. Kane, A. L. Ionin, M. S. Lee, R. V. Chopdekar, J. M. Christiansen-Salameh, D. A. Gilbert, A. J. Grutter, P. D. Murray, M. V. Holt, Z. Cai, K. Liu, Y. Takamura, and R. Kukreja, *Phys. Rev. Mater.* **3**, 082001(R) (2019).

- [15] A. J. Grutter, D. A. Gilbert, U. S. Alaan, E. Arenholz, B. B. Maranville, J. A. Borchers, Y. Suzuki, K. Liu, and B. J. Kirby, *Appl. Phys. Lett.* **108**, 082405 (2016).
- [16] P. D. Murray, D. A. Gilbert, A. J. Grutter, B. J. Kirby, D. Hernández-Maldonado, M. Varela, Z. E. Brubaker, W. L. N. C. Liyanage, R. V. Chopdekar, V. Taufour, R. J. Zieve, J. R. Jeffries, E. Arenholz, Y. Takamura, J. A. Borchers, and K. Liu, *ACS Appl. Mater. Interfaces* **12**, 4741 (2020).
- [17] N. Lu, P. Zhang, Q. Zhang, R. Qiao, Q. He, H.-B. Li, Y. Wang, J. Guo, D. Zhang, Z. Duan, Z. Li, M. Wang, S. Yang, M. Yan, E. Arenholz, S. Zhou, W. Yang, L. Gu, C.-W. Nan, J. Wu, Y. Tokura, and P. Yu, *Nature* **546**, 124 (2017).
- [18] V. R. Nallagatla, T. Heisig, C. Baeumer, V. Feyer, M. Jugovac, G. Zamborlini, C. M. Schneider, R. Waser, M. Kim, C. U. Jung, and R. Dittmann, *Adv. Mater.* **31**, 1903391 (2019).
- [19] C. Tassel and H. Kageyama, *Chem. Soc. Rev.* **41**, 2025 (2012).
- [20] N. Ichikawa, M. Iwanowska, M. Kawai, C. Calers, W. Paulus, and Y. Shimakawa, *Dalton Trans.* **41**, 10507 (2012).
- [21] Y. Tsujimoto, C. Tassel, N. Hayashi, T. Watanabe, H. Kageyama, K. Yoshimura, M. Takano, M. Ceretti, C. Ritter, and W. Paulus, *Nature* **450**, 1062 (2007).
- [22] Q. Zhang, X. He, J. Shi, N. Lu, H. Li, Q. Yu, Z. Zhang, L.-Q. Chen, B. Morris, Q. Xu, P. Yu, L. Gu, K. Jin, and C.-W. Nan, *Nat. Commun.* **8**, 104 (2017).
- [23] S. K. Pandey, *Phys. Rev. B* **81**, 035114 (2010).
- [24] Q. Li, X. Yuan, L. Xing, and M. Xu, *Sci. Rep.* **6**, 27712 (2016).
- [25] J. Wu, J. W. Lynn, C. J. Glinka, J. Burley, H. Zheng, J. F. Mitchell, and C. Leighton, *Phys. Rev. Lett.* **94**, 037201 (2005).
- [26] T. Ishihara, *Perovskite Oxide for Solid Oxide Fuel Cells* (Springer, Boston, MA, USA, 2009).
- [27] Z. Zhang, F. Zuo, C. Wan, A. Dutta, J. Kim, J. Rensberg, R. Nawrodt, H. H. Park, T. J. Larrabee, X. Guan, Y. Zhou, S. M. Prokes, C. Ronning, V. M. Shalaev, A. Boltasseva, M. A. Kats, and S. Ramanathan, *Phys. Rev. Appl.* **7**, 034008 (2017).
- [28] M.-H. Lee, Y. Kalcheim, J. d. Valle, and I. K. Schuller, *ACS Appl. Mater. Interfaces* **13**, 887 (2021).
- [29] M. Bjorck and G. Andersson, *J. Appl. Crystallogr.* **40**, 1174 (2007).
- [30] Y. Jia, R. V. Chopdekar, E. Arenholz, A. T. Young, M. A. Marcus, A. Mehta, and Y. Takamura, *Phys. Rev. B* **92**, 094407 (2015).
- [31] A. Bianconi, D. Jackson, and K. Monahan, *Phys. Rev. B* **17**, 2021 (1978).
- [32] P. Giannozzi *et al.*, *J. Phys. Condens. Matter* **29**, 465901 (2017).
- [33] P. Giannozzi *et al.*, *J. Phys. Condens. Matter* **21**, 395502 (2009).
- [34] S. Zhang and G. Galli, *npj Comput. Mater.* **6**, 170 (2020).
- [35] J. P. Perdew, K. Burke, and M. Ernzerhof, *Phys. Rev. Lett.* **77**, 3865 (1996).
- [36] A. Dal Corso, *Comput. Mater. Sci.* **95**, 337 (2014).
- [37] A. Jain, S. P. Ong, G. Hautier, W. Chen, W. D. Richards, S. Dacek, S. Cholia, D. Gunter, D. Skinner, G. Ceder, and K. A. Persson, *APL Mater.* **1**, 011002 (2013).
- [38] H. J. Monkhorst and J. D. Pack, *Phys. Rev. B* **13**, 5188 (1976).
- [39] See Supplemental Material at <http://link.aps.org/supplemental/10.1103/PhysRevMaterials.5.064416> for additional information justifying the results and discussion included in the main texts.
- [40] T. Ishihara, in *Springer Handbook of Electronic and Photonic Materials*, edited by S. Kasap, and P. Capper (Springer International Publishing, Cham, 2017), pp. 1.
- [41] X. Liu, L. Zhang, Y. Zheng, Z. Guo, Y. Zhu, H. Chen, F. Li, P. Liu, B. Yu, X. Wang, J. Liu, Y. Chen, and M. Liu, *Adv. Sci.* **6**, 1801898 (2019).
- [42] Y. Chen, D. D. Fong, F. W. Herbert, J. Rault, J.-P. Rueff, N. Tsvetkov, and B. Yildiz, *Chem. Mater.* **30**, 3359 (2018).
- [43] Yu Chen and S. B. Adler, *Chem. Mater.* **17**, 4537 (2005).
- [44] S. M. Ansari, R. D. Bhor, K. R. Pai, D. Sen, S. Mazumder, K. Ghosh, Y. D. Kolekar, and C. V. Ramana, *Appl. Surf. Sci.* **414**, 171 (2017).
- [45] H. Yoon, A. Xu, G. E. Sterbinsky, D. A. Arena, Z. Wang, P. W. Stephens, Y. S. Meng, and K. J. Carroll, *PCCP* **17**, 1070 (2015).
- [46] E. Rauwel, S. Al-Arag, H. Salehi, C. O. Amorim, F. Cuisinier, M. Guha, M. S. Rosario, and P. Rauwel, *Int. J. Nanomed.* **15**, 7051 (2020).
- [47] M. Bahout, P. B. Managutti, V. Dorcet, A. Le Gal La Salle, S. Paofai, and T. C. Hansen, *J. Mater. Chem. A* **8**, 3590 (2020).
- [48] G. Yang, W. Zhou, M. Liu, and Z. Shao, *ACS Appl. Mater. Interfaces* **8**, 35308 (2016).
- [49] N. V. Kuleshov, V. P. Mikhailov, V. G. Scherbitsky, P. V. Prokoshin, and K. V. Yumashev, *J. Lumin.* **55**, 265 (1993).
- [50] K. Ravindranadh, B. Babu, M. C. Rao, J. Shim, C. Venkata Reddy, and R. V. S. S. N. Ravikumar, *J. Mater. Sci. Mater. Electron.* **26**, 6667 (2015).
- [51] N. Sabir, W. Qayyum, S. Z. Hussain, I. Hussain, and F. Amin, Photoluminescence properties of Co and Ni co-doped CdS/ZnS core/shell nanoparticles, in *Colloidal Nanoparticles for Biomedical Applications XIII*, Proceedings of SPIE, Vol. 10507 (SPIE, San Francisco, California, United States, 2018), pp. 1050705.
- [52] T. N. Nunley, T. I. Willett-Gies, J. A. Cooke, F. S. Manciu, P. Marsik, C. Bernhard, and S. Zollner, *J. Vac. Sci. Technol. A* **34**, 051507 (2016).
- [53] R. V. Chopdekar, M. Liberati, Y. Takamura, L. F. Kourkoutis, J. S. Bettinger, B. B. Nelson-Cheeseman, E. Arenholz, A. Doran, A. Scholl, D. A. Muller, and Y. Suzuki, *J. Magn. Magn. Mater.* **322**, 2915 (2010).
- [54] A. M. Kane, I. T. Chiu, N. J. Ahlm, R. V. Chopdekar, A. T. N'Diaye, E. Arenholz, A. Mehta, V. Lauter, and Y. Takamura, *ACS Appl. Mater. Interfaces* **12**, 45437 (2020).
- [55] M. Merz, P. Nagel, C. Pinta, A. Samartsev, H. v. Löhneysen, M. Wissinger, S. Uebe, A. Assmann, D. Fuchs, and S. Schuppler, *Phys. Rev. B* **82**, 174416 (2010).
- [56] B. Bechlers, D. M. D'Alessandro, D. M. Jenkins, A. T. Iavarone, S. D. Glover, C. P. Kubiak, and J. R. Long, *Nat. Chem.* **2**, 362 (2010).
- [57] J. H. Lee, W. S. Choi, H. Jeon, H. J. Lee, J. H. Seo, J. Nam, M. S. Yeom, and H. N. Lee, *Sci. Rep.* **7**, 16066 (2017).
- [58] N. Biškup, J. Salafranca, V. Mehta, M. P. Oxley, Y. Suzuki, S. J. Pennycook, S. T. Pantelides, and M. Varela, *Phys. Rev. Lett.* **112**, 087202 (2014).
- [59] B. Morcos, P. Lecante, R. Morel, P.-H. Haumesser, and C. C. Santini, *Langmuir* **34**, 7086 (2018).
- [60] K. S. Rao, T. Balaji, Y. Lingappaa, M. R. P. Reddy, and T. L. Prakash, *J. Exp. Nanosci.* **8**, 162 (2013).
- [61] B. J. Chen, K. Zhao, Z. Deng, W. Han, J. L. Zhu, X. C. Wang, Q. Q. Liu, B. Frandsen, L. Liu, S. Cheung, F. L. Ning, T. J. S. Munsie, T. Medina, G. M. Luke, J. P. Carlo, J. Munevar, Y. J. Uemura, and C. Q. Jin, *Phys. Rev. B* **90**, 155202 (2014).
- [62] S. K. Bose, J. Kudrnovský, V. Drchal, and I. Turek, *Phys. Rev. B* **84**, 174422 (2011).



- [63] T. Ma, J. Gou, S. Hu, X. Liu, C. Wu, S. Ren, H. Zhao, A. Xiao, C. Jiang, X. Ren, and M. Yan, *Nat. Commun.* **8**, 13937 (2017).
- [64] A. Maignan, D. Pelloquin, C. Martin, M. Hervieu, and B. Raveau, *J. Mater. Chem.* **12**, 1009 (2002).
- [65] T. Motohashi, V. Caignaert, V. Pralong, M. Hervieu, A. Maignan, and B. Raveau, *Appl. Phys. Lett.* **86**, 192504 (2005).
- [66] A. Muñoz, C. de la Calle, J. A. Alonso, P. M. Botta, V. Pardo, D. Baldomir, and J. Rivas, *Phys. Rev. B* **78**, 054404 (2008).
- [67] G. van der Laan, B. T. Thole, G. A. Sawatzky, J. B. Goedkoop, J. C. Fuggle, J.-M. Esteva, R. Karnatak, J. P. Remeika, and H. A. Dabkowska, *Phys. Rev. B* **34**, 6529 (1986).
- [68] G. van der Laan, E. Arenholz, R. V. Chopdekar, and Y. Suzuki, *Phys. Rev. B* **77**, 064407 (2008).
- [69] S. Czekaj, F. Nolting, L. J. Heyderman, P. R. Willmott, and G. van der Laan, *Phys. Rev. B* **73**, 020401(R) (2006).
- [70] J. Schwerdt, G. Goya, M. P. Calatayud, C. Herenu, P. Reggiani, and R. Goya, *Curr. Gene Ther.* **12**, 116 (2012).
- [71] V. A. Bautin, A. G. Seferyan, M. S. Nesmeyanov, and N. A. Usov, *AIP Adv.* **7**, 045103 (2017).